

Improved Electrochemical Performance of $\text{LiMn}_{0.6}\text{Fe}_{0.4}\text{PO}_4$ via Chitosan-Derived Nitrogen-Doped Carbon Coating

Jiawang Zhang,^[a] Youming Liu,^[a] Baofeng Wang,^[a] and Weifeng Yao^{*[a, b, c]}

The olivine-type compound $\text{LiMn}_{x}\text{Fe}_{1-x}\text{PO}_4$ (LMFP) combines the advantageous characteristics of LiFePO_4 and LiMnPO_4 , including high energy density, extended cycle life, eco-friendliness, and cost-effectiveness. However, its application is limited by certain challenges such as low electronic conductivity and stability issues related to the Jahn-Teller effect induced by Mn^{3+} , which hinder its scalability. Here, we introduce an innovative approach by applying nitrogen-doped carbon layers, derived from chitosan as both a carbon and nitrogen sources, to encapsulate

LMFP. This encapsulation significantly improves LMFP's electrochemical performance compared to those using sucrose-derived carbon coatings. The LMFP cathode with nitrogen-doped carbon coating exhibits a specific capacity of 156.8 mAh/g at 0.1 C, achieved a first-cycle Coulombic efficiency of 96.8%, and maintained a capacity retention rate of 94.6% after 200 cycles at 1 C. This new method of employing chitosan for producing nitrogen-doped carbon coatings holds great promise for enhancing the usability of LMFP in broader applications.

1. Introduction

Lithium-ion batteries, widely adopted as chemical power source, have become integral to electric vehicles, digital devices, and various electric tools, owing to their high specific energy, specific power and extended cycle life.^[1-2] LiFePO_4 , featuring an olivine structure, gained significant attention since 1997 due to its notable theoretical capacity (170 mAh/g), safety attributes, and cost-effectiveness.^[3-4] However, the growing demands for increased range in electric vehicles has highlighted the limitations of LiFePO_4 (578 Wh/kg) in meeting energy density requirements, primarily due to its lower redox potential (3.4 V vs. Li/Li⁺).^[5] In contrast, LiMnPO_4 presents a higher redox potential (4.1 V vs. Li/Li⁺)^[6-8] resulting in a substantial 21% increase in energy density (700 Wh/kg) compared to LiFePO_4 .^[9] Despite this promising potential, LiMnPO_4 faces challenges such as low electronic conductivity, ion diffusion coefficient, and the impediment of the Jahn Teller effect on commercialization.^[10-11]

Addressing these challenges, the exploration of a $\text{LiMn}_{x}\text{Fe}_{1-x}\text{PO}_4$ (LMFP) solid solution, achieved by incorporating Mn^{2+} with a similar radius to Fe^{2+} , has gained global attention.^[12-13] However, the increase in bandgap and congestion within LMFP necessitate improvements in electronic and ion conductivity.^[14]

Furthermore, the intrinsic Jahn-Teller effect of $\text{Mn}^{2+/3+}$ poses additional constraints on the reaction kinetics of LMFP cathode materials during rapid charging/discharging processes.^[15] Recognizing carbon coating as an effective method to enhance electrical conductivity, there is a need to identify suitable materials for modifying LMFP to further enhance its electrochemical performance.

Recent researches underscore nitrogen doping as a promising strategy for improving the conductivity and electrochemical performance of carbon materials.^[16] Nitrogen doping has been demonstrated to decrease the electron transfer distance between the active material and the electrolyte, thereby facilitating the rapid diffusion of electrolyte ions.^[17-18] Ding et al.^[19] observed that nitrogen doping introduces a significant number of defects in the SP^2 carbon structure, which proves advantageous for the diffusion of lithium ions at the interface. Moreover, Fu and Sevilla^[20-21] demonstrated that nitrogen-doped carbon materials can significantly reduce charge transfer resistance in supercapacitors. Common methods for nitrogen-doped carbon synthesis include CVD, solvothermal, heat treatment, and plasma treatment. However, these nitrogen-doping methods require specialized equipment, intricate procedures, and are cost-intensive. Therefore, there is a necessity to explore low-cost and low-temperature alternatives for nitrogen-doped carbon materials.

Chitosan is an inexpensive and abundant renewable biomass resource with broad application potential in the synthesis of nitrogen-doped nanocomposites. Due to the characteristic $-\text{NH}_2$ functional group of chitosan, when it decomposes at elevated temperature to form amorphous carbon and graphene nanosheets, the nitrogen atoms generated by the decomposition of NH_2 groups are incorporated into the carbon material skeleton, forming nitrogen doped carbon materials.^[22] In contrast to methods such as chemical vapor deposition and heat treatment, this chitosan-derived approach offers a simpler and more economical synthesis pathway that is well aligned with environmentally friendly principles.^[23] In the

[a] J. Zhang, Y. Liu, B. Wang, W. Yao

Shanghai Key Laboratory of Materials Protection and Advanced Materials in Electric Power, Shanghai University of Electric Power, 201306 Shanghai, PR China

E-mail: yaowefeng@shiep.edu.cn

[b] W. Yao

Shanghai Institute of Pollution Control and Ecological Security, 200092 Shanghai, PR China

[c] W. Yao

Shanghai Engineering Research Center of Heat-exchange System and Energy Saving, Shanghai University of Electric Power, 201306 Shanghai, PR China

 Supporting information for this article is available on the WWW under <https://doi.org/10.1002/batt.202400105>

field of lithium batteries, chitosan is often used as a water-soluble binder for anodes.^[24] Yue et al.^[25] highlighted chitosan as an excellent water-soluble binder for lithium-ion batteries, demonstrating commendable electrochemical performance. Compared to polyvinylidene fluoride binder, lithium-ion batteries prepared with chitosan water-soluble binder exhibit improved rate performance, cycle life, and coulombic efficiency. However, there is limited literature on the use of chitosan as a carbon source to modify LMFP.

The current investigation focuses on nitrogen-doped carbon coating of LMFP using chitosan as both carbon and nitrogen source, marking the first exploration in this field. The results show that the incorporation of a nitrogen-doped carbon layer derived from chitosan remarkably enhances the performance of LMFP, surpassing that of sucrose-coated LMFP material. Specifically, it exhibits a specific capacity of 156.8 mAh/g at 0.1 C, coupled with a coulomb efficiency of 96.8% and an impressive capacity retention rate of over 94.6% after more than 200 cycles. This study provides a convenient approach to the fabrication of high-performance LMFP materials.

Experimental

Synthesis of $\text{LiMn}_{0.6}\text{Fe}_{0.4}\text{PO}_4$

The $\text{LiMn}_{0.6}\text{Fe}_{0.4}\text{PO}_4$ cathode material was synthesized using a liquid-phase method. Initially, 3 mmol of $\text{LiOH} \cdot \text{H}_2\text{O}$ was dissolved in 15 ml of deionized water. Subsequently, 10 mmol of H_3PO_4 solution was slowly added to the $\text{LiOH} \cdot \text{H}_2\text{O}$ solution under magnetic stirring, resulting in a white solution. Simultaneously, 6 mmol $\text{MnSO}_4 \cdot \text{H}_2\text{O}$ and 4 mmol $\text{FeSO}_4 \cdot 7\text{H}_2\text{O}$ were dissolved together in 15 ml of deionized water, forming a yellow transparent metal salt solution. The white solution was then added to the metal salt solution under magnetic stirring, stirred for 1 hour, and transferred to a Teflon-lined stainless steel autoclave. The autoclave was maintained at 180°C for 10 h in an electric oven. The precipitate was washed by centrifugation with deionized water and dried in a vacuum oven at 60°C for 12 hours to yield $\text{LiMn}_{0.6}\text{Fe}_{0.4}\text{PO}_4$.

Synthesis of $\text{LiMn}_{0.6}\text{Fe}_{0.4}\text{PO}_4/\text{C}$

To begin, dissolve 0.3 g of sucrose in deionized water under magnetic stirring conditions. Then, add 2 g of LMFP to the solution and subject it to ball milling at 200 rpm for 2 hours using a planetary ball mill. Use a spray dryer to spray granulate the resulting slurry, yielding solid powder. Finally, anneal the solid powder at 700°C in a nitrogen atmosphere for 6 hours. The resulting material carbon coated LMFP is named as LMFP/C.

Synthesis of $\text{LiMn}_{0.6}\text{Fe}_{0.4}\text{PO}_4/\text{NC}$

Start by preparing a 5% acetic acid solution, into which 0.6 g of chitosan is dissolved under magnetic stirring. After stirring for 0.5 hours, a light yellow transparent sol is obtained. Add 2 g LMFP powder to the sol and proceed with ball milling at 200 rpm for 2 hours using a planetary ball mill. The mixture is then spray-dried to obtain a solid powder, which is annealed in a nitrogen atmosphere at 700°C for 6 hours, resulting in nitrogen doped carbon coated LMFP, denoted as LMFP/NC. To investigate the impact of chitosan quantities, repeat the process using 0.4 g and

0.8 g chitosan, producing materials named LMFP/NC-1 and LMFP/NC-2, respectively. For better visualization and comprehension, a schematic diagram of the synthesis process for LMFP/NC is presented in Figure S1.

Structural Characterization

The sample's phase composition was analysed using an X-ray diffractometer (D8Advance Bruker AXS). The morphology and microstructure were characterised using scanning electron microscopy (SEM, JEM-7800F) and transmission electron microscopy (TEM, JEM-2100). The composition and valence states of surface elements were analysed using X-ray photoelectron spectroscopy (Thermo Scientific K-Alpha). The sample's microstructures were analysed using a Raman microscopic instrument (Horiba OLYMPUS BX41).

Electrochemical Measurements

To assess its electrochemical performance, we used the CR2025 button battery. The positive electrode material was mixed with carbon black (Super P) and polyvinylidene fluoride (PVDF) in a weight ratio of 8:1:1 in N-Methylpyrrolidone (NMP) to create a uniform slurry. The slurry was then subjected to planetary ball milling for 2 hours and adjusted to the appropriate viscosity using NMP. The electrode was formed by applying the slurry onto aluminum foil and drying it in a vacuum oven at 80°C for 12 hours. The CR2025 battery was assembled in an argon gas-filled glove box, using lithium metal sheets as counter electrodes, Celgard as separator, and 1 mol L⁻¹ LiPF_6 as electrolyte (EC:DEC:EMC, 1:1:1, V/V/V). To evaluate the synthesized samples, we conducted tests on specific capacities, rate performances, and cycle life using a LANDCT2001 A within the voltage range of 2.5–4.2 V. We obtained cyclic voltammetry (CV) and electrochemical impedance spectroscopy (EIS) spectrum using a CHI660E electrochemical workstation. The EIS recordings covered a frequency range of 100 kHz–0.01 Hz with an AC signal amplitude of 5 mV. The CV test was conducted with a voltage range of 2.5–4.2 V and a scanning rate of 0.1 mV s⁻¹. All tests were performed at room temperature.

2. Results and Discussion

Figure 1 shows the XRD diffraction patterns of LMFP, LMFP/C, and LMFP/NC, which closely align with the diffraction patterns of olivine LiMnPO_4 (JCPDS # 74-0375) with Pmnb (62) spatial group.^[26] This alignment indicates the successful preparation of high-purity and well-crystallized LMFP through the liquid-phase method, with the crystal structure of LMFP remaining unchanged during the modification process. Notably, crystalline carbon diffraction peaks were absent in both LMFP/C and LMFP/NC. The primary reason for this absence is the low sucrose and chitosan content in the modified samples.

Figure 2 shows the SEM characterization of LMFP and LMFP/NC. In Figures 2 (a) and 2 (b), the LMFP prepared using the liquid-phase method consists of numerous nanorods with lengths ranging from 100 to 300 nm. The microspheres, formed by spray drying, self assemble from primary nanoparticles with a particle size of 2–3 μm . The TEM image of LMFP/NC is presented in Figure 3 (a), revealing the formation of an amorphous carbon layer approximately 2.4 nm thick on the

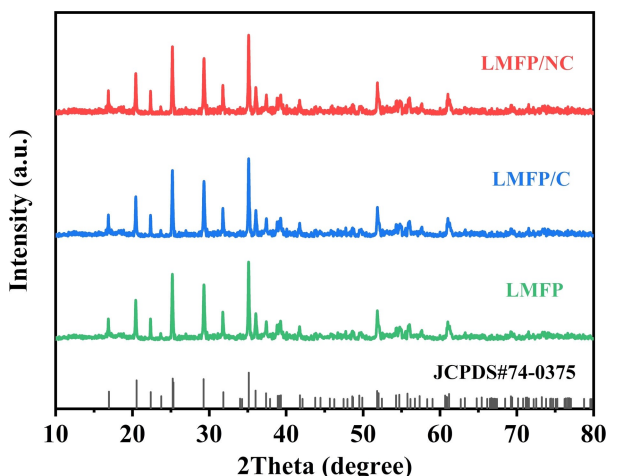


Figure 1. XRD diffraction patterns of LMFP, LMFP/C, LMFP/NC.

surface of LMFP/NC particles. The material's conductivity is enhanced by the carbon layer resulting from chitosan carbonization at elevated temperatures. Beneath the carbon layer, the material exhibits well-defined lattice stripes, indicating robust crystal crystallinity. HRTEM analysis reveals the lattice fringes with a d-spacing of 0.3453 nm, corresponding to the (021) plane of LMFP. Figures 3 (b) to (f) display the EDS spectra of LMFP/NC, showcasing the uniform distribution of each element.

Figure 4 presents the XPS spectrum of LMFP/NC. The spectrum in Figure 4 (a) shows the presence of Li, Mn, Fe, O, P, C, and N elements in the LMFP/NC sample. The high-resolution

spectrum shown in Figure 4 (b) corresponds to the carbon element (C 1s) derived from the annealing products of chitosan.^[27] The four peaks fitted in the C 1s spectrum correspond to C–C (284.8 eV), C=N (285.9 eV), and C–N- (288.6 eV).^[28] The N 1s XPS spectrum of the LMFP/NC sample is depicted in Figure 4 (c). The N 1s spectrum can be divided into three peaks representing pyridinic N, pyrrolic N and graphitic N at 398.98, 400.29 and 402.7 eV, respectively.^[28] This confirms the presence of N derived from the -NH₂ functional group of chitosan. It has been reported that defects introduced by N-doping are advantageous for the diffusion of lithium ions and contribute to the improved electrochemical performance of the material.^[29]

Figure S2 displays the Raman spectra of LMFP/C and LMFP/NC, which were analyzed to determine their degree of graphitization. The spectra show intense bands at approximately 1378 and 1570 cm⁻¹, corresponding to the D and G bands of carbon. The D-band is associated with carbon defects and disorder, while the G-band indicates ordered sp² carbon. The I_D/I_G peak intensity ratio is a useful indicator for estimating the level of graphitization in carbon materials.^[30] Research has shown that polysaccharides such as chitosan, cellulose, peptidoglycan, and starch tend to form graphene nanoribbons during pyrolysis, resulting in a higher degree of graphitization.^[22] The evidence suggests that LMFP/NC ($I_D/I_G=0.90$) has a higher degree of graphitization than LMFP/C ($I_D/I_G=1.1$), which is advantageous for electron transfer.

Figure 5(a) shows the charge-discharge curves of LMFP/NC prepared at different carbonization temperatures under a rate of 0.1 C. The crystallinity of LMFP/NC is influenced by the

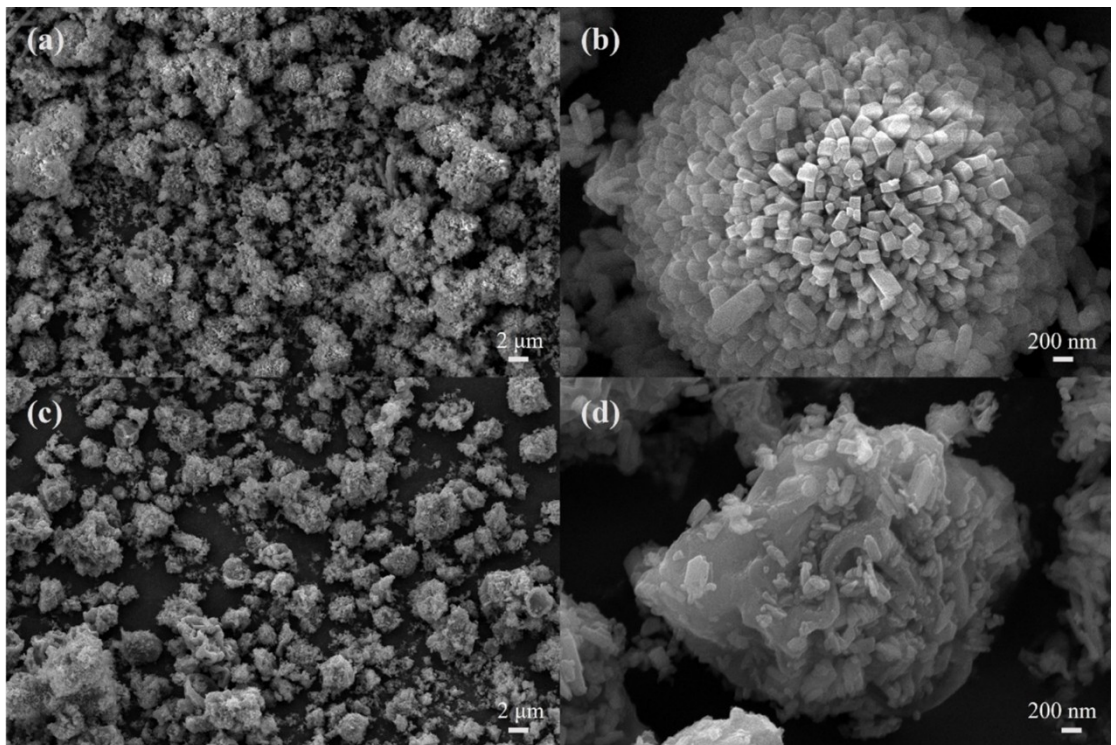


Figure 2. (a), (b) SEM images of LMFP; (c), (d) SEM images of LMFP/NC.

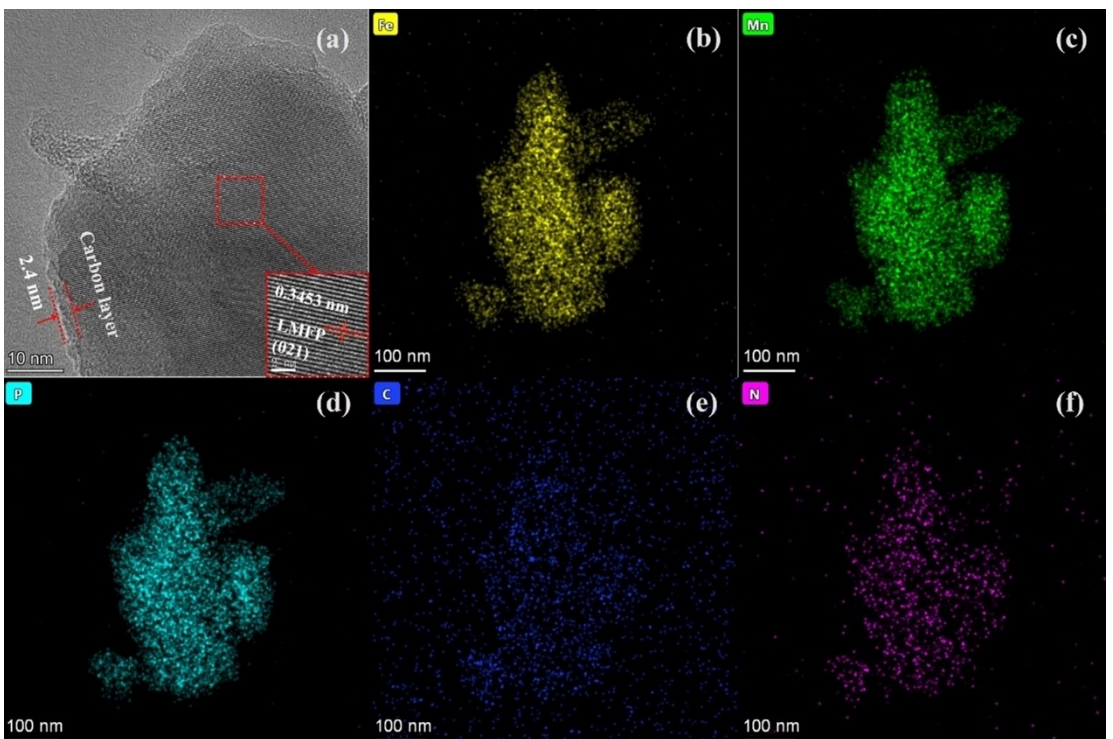


Figure 3. (a) TEM image of LMFP/NC, (b)~(f) EDS images of LMFP/NC.

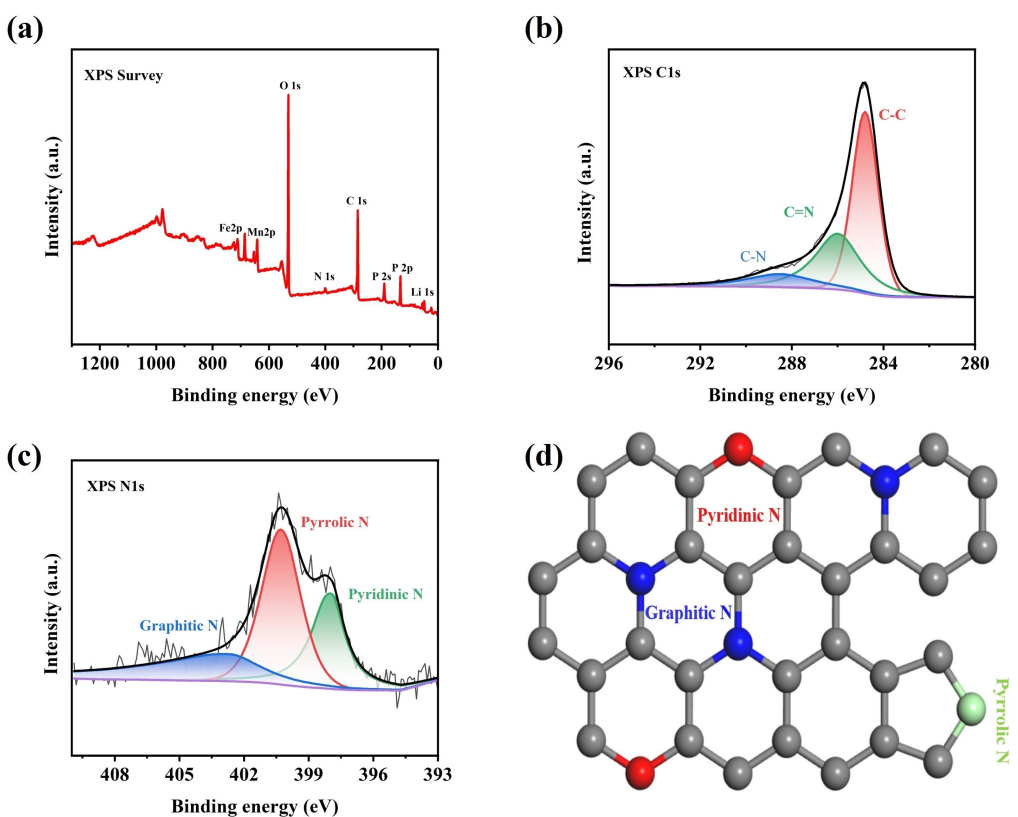


Figure 4. (a) XPS spectrum of LMFP/NC, (b) C1s spectrum, (c) N1s spectrum, (d) Various forms of N element in chitosan after annealing.

carbonization temperature, showing an improvement as the temperature increases. This increase in crystallinity aids in

developing more complete crystal structures and enhances the diffusion of lithium ions within the material. Specifically, LMFP/

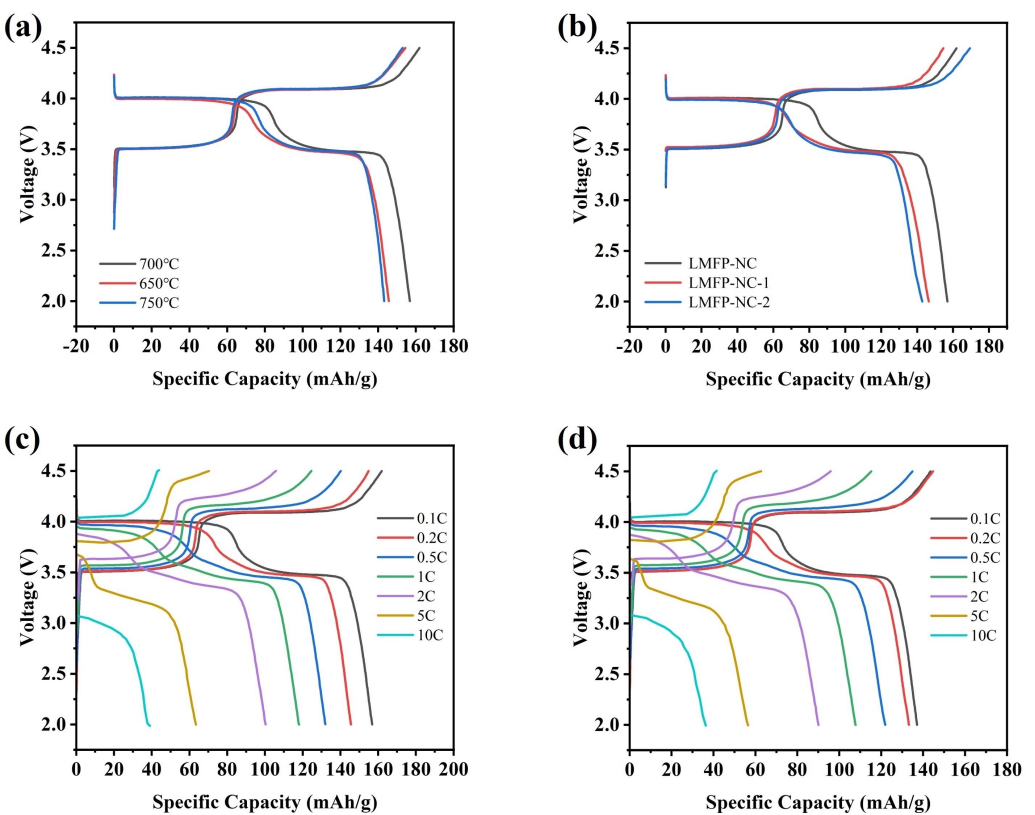


Figure 5. Charge-discharge curves of LMFP/NC and LMFP/C under various conditions: (a) LMFP/NC at different carbonization temperatures, (b) LMFP/NC with different chitosan doping amounts, (c) LMFP/NC at different rates, and (d) LMFP/C at different rates.

NC samples treated at 700 °C and 750 °C display superior crystallinity compared to those treated at 650 °C. However, a carbonization temperature of 750 °C, while favorable for crystal formation, tends to induce sintering. The SEM image of LMFP/NC-750 is presented in Figure S3. This can lead to particle agglomeration, elongating the diffusion pathway for lithium ions and negatively impacting material performance. Therefore, LMFP/NC processed at 700 °C exhibits the optimal specific capacity, balancing enhanced crystallinity without the adverse effects of excessive sintering.

In Figure 5(b), the charge-discharge curves of different cathodes prepared with varying ratios of LMFP and chitosan at 0.1 C indicate that the optimal ratio is 10:3. The cathode with the highest effectiveness achieves a discharge capacity of 156.8 mAh/g at 0.1 C. Figures 5(c) and 5(d) show the charge-discharge curves of LMFP/NC and LMFP/C at different rates. LMFP/NC has discharge capacities of 156.8, 145.6, 132.0, 118.0, 100.3, 63.4 and 39.1 mAh/g at rates of 0.1 C, 0.2 C, 0.5 C, 1 C, 2 C, 5 C and 10 C, respectively. Meanwhile, LMFP/C delivers discharge capacities of 137.1, 133.2, 121.9, 107.8, 90.1, 56.5 and 36.3 mAh/g at the corresponding rates. This shows that an optimal level of carbon-doped nitrogen coating improves the charging and discharging performance of the material. As the rate increases, the current density also increases, resulting in greater electrode polarization and a gradual reduction in discharge specific capacity. Additionally, the voltage platform shortens at high current density, indicating increased oxidation-

reduction polarization and reduced charge-discharge reversibility.

Figure 6(a) shows the rate capabilities of LMFP/NC and LMFP/C, with LMFP/NC performing better at different rates. Different from that in Figure 5(c), LMFP/NC in Figure 6(a) undergoes five charge and discharge cycles at each rate. Each cycle exacerbates the polarization of the battery, resulting in a progressive decline in its discharge specific capacity. Consequently, as the current density and the number of charge-discharge cycles increase, LMFP/NC exhibits improved rate performance in Figure 5(c) compared to Figure 6(a). The cyclic performance after 200 cycles at 1 C is illustrated in Figure 6(b). The initial discharge specific capacities at 1 C are 122.2 mAh/g for LMFP/NC and 114.6 mAh/g for LMFP/C, respectively. After 200 cycles, the capacity retention rates were 94.6% and 92.6%, respectively, demonstrating improved discharge performance and cycling stability. Table 1 compares the electrochemical performance of LMFP/NC composite materials with those of the same material previously reported, highlighting its excellent electrochemical performance.

Figure 6(c) presents the cyclic voltammetry (CV) curves of LMFP/NC and LMFP/C obtained at a scanning rate of 0.1 mV/s within the 2.0–4.5 V range. Two pairs of redox peaks are evident in the 3.3–3.7 V and 3.8–4.2 V range, corresponding to the redox reactions of $\text{Fe}^{2+}/\text{Fe}^{3+}$ and $\text{Mn}^{2+}/\text{Mn}^{3+}$, respectively.^[31] It is worth noting that the peak potential difference of LMFP/NC ($\text{Fe}^{2+}/\text{Fe}^{3+}$: 0.239 V, $\text{Mn}^{2+}/\text{Mn}^{3+}$: 0.352 V) is smaller than that of

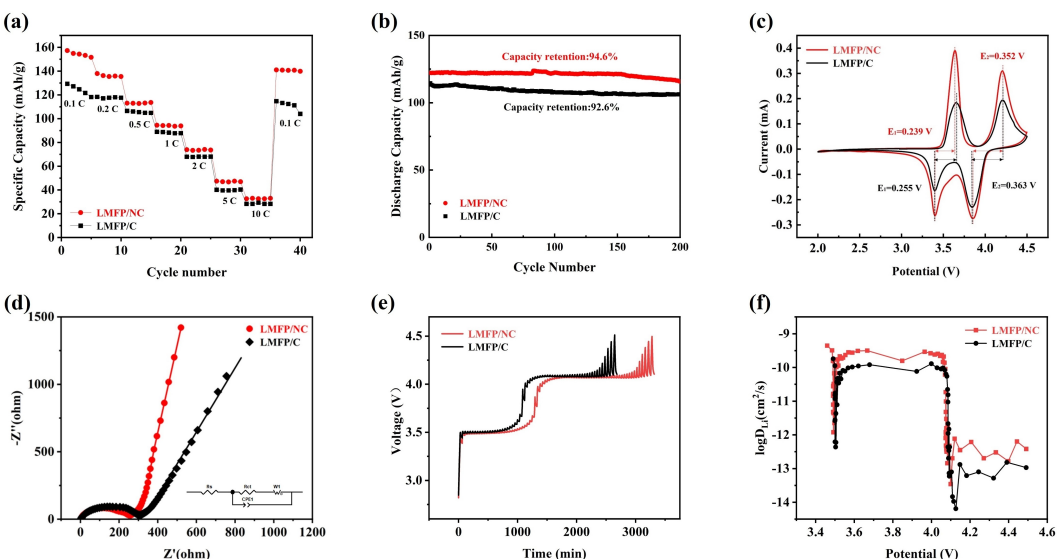


Figure 6. Comparative Analysis of LMFP/NC and LMFP/C: (a) Rate capability, (b) Cycling performance and charge-discharge curves, (c) CV curves at 0.1 mV/s, (d) Nyquist plots, (e) GITT curves during charging, (f) the $\log D_{Li}$ -Potential.

Table 1. Comparison of the electrochemical performances of LMFP cathode in the voltage of 2.5–4.2 V at 0.1 C.

Samples	Carbon Source	Capacity (mAh/g) at 0.1 C	Reference
LiMn _{0.6} Fe _{0.4} PO ₄ /C	glucose	156	[38]
LiMn _{0.5} Fe _{0.5} PO ₄ /C	glucose	152	[39]
LiMn _{0.8} Fe _{0.2} PO ₄ /C	sucrose	136	[13]
LiMn _{0.7} Fe _{0.3} PO ₄ /C	graphene oxide	153	[40]
LiMn _{0.5} Fe _{0.5} PO ₄ /C	resorcinol-formaldehyde	155.4	[41]
LiMn _{0.6} Fe _{0.4} PO ₄ /NC	Chitosan	156.8	This work

LMFP/C ($Fe^{2+}/Fe^{3+} 0.255$ V, $Mn^{2+}/Mn^{3+} 0.363$ V). This difference shows that LMFP/NC has lower electrochemical polarization and better kinetic properties than LMFP/C. Figure 6(d) shows the equivalent circuit model employed for impedance spectrum analysis and the Nyquist plots of LMFP/NC and LMFP/C. The Nyquist curve encompasses a semicircle in the mid to high frequency region, representing the charge-transfer resistance (R_{ct}), and a slope line in the low frequency region, associated with the Li^+ diffusion process.^[32–34] In Figure 6(d), the R_{ct} values for LMFP/NC and LMFP/C are 223.3 and 301.6 Ω , respectively. This indicates that nitrogen-doped carbon materials can mitigate the resistance in lithium-ion batteries, highlighting the superior electrochemical performance of LMFP/NC.

To elucidate the factors behind the superior electrochemical performance of LMFP/NC, the reaction kinetics were further studied using Galvanostatic Intermittent Titration Technique (GITT). Figure 6(e) shows the GITT curves for both LMFP/NC and LMFP/C during the charging process. From these curves, the Li^+ diffusion coefficient D_{Li} in the positive electrode was calculated using the following equation:^[35–37]

$$D_{Li} = \frac{4}{\pi\tau} \left(\frac{n_m V_m}{S} \right)^2 \left[\frac{\Delta E_s}{\Delta E_t} \right]^2$$

where τ is the galvanic titration time, n_m is the number of moles, V_m is the molar volume, S is the surface area of the cathode, ΔE_s and ΔE_t represent the stabilized voltage variation after the relaxation stage and the instantaneous voltage change during the individual current pulse, respectively.

The D_{Li} values for LMFP/NC and LMFP/C were calculated at varied voltages and are shown in Figure 6(f). Notably, LMFP/NC exhibits a larger D_{Li} value compared to LMFP/C, especially at elevated voltage. For instance, at 4.2 V, the D_{Li} value of LMFP/NC is 6.11×10^{-13} cm²/s, much greater than the 2.20×10^{-13} cm²/s observed for LMFP/C. This suggests that LMFP/NC facilitates quicker Li^+ diffusion and exhibits superior electrochemical performance, corroborating the findings from constant current charge-discharge tests.

3. Conclusions

LMFP precursors were synthesized using a liquid-phase method, followed by the preparation of carbon coated LMFP/NC and LMFP/C through a straightforward spray-drying route. The study suggests that using chitosan as a carbon source results in nitrogen defects formed after carbonization, promoting the diffusion of lithium ions and enhancing electrochemical

performance. Simultaneously, the carbonized chitosan exhibits a higher degree of graphitization, which facilitates electron transfer. In comparison to LMFP/C, LMFP/NC displays reduced impedance ($R_{ct}=223.3\ \Omega$) and a higher lithium ion diffusion coefficient ($6.11\times10^{-13}\ \text{cm}^2/\text{s}$). LMFP/NC demonstrates an increase in capacity from 137.1 mAh/g at 0.1 C to 156.8 mAh/g, with a capacity retention rate of 94.6% after 200 cycles at 1 C.

Acknowledgements

This work was financially supported by the Science and Technology Commission of Shanghai Municipality (19DZ2271100), and the Shanghai Committee of Science and Technology (17DZ2282800).

Conflict of Interests

The authors declare no conflict of interest.

Data Availability Statement

The data that support the findings of this study are available from the corresponding author upon reasonable request.

Keywords: $\text{LiMn}_{x}\text{Fe}_{1-x}\text{PO}_4$ • Lithium-ion batteries • Chitosan • Anode • Nitrogen-doped carbon

- [1] H. Ji, J. Wang, J. Ma, H.-M. Cheng, G. Zhou, *Chem. Soc. Rev.* **2023**, *52*, 8194–8244.
- [2] C. Li, X. Yu, C. Liao, Z. Cui, J. Zhu, M. Gao, W. Wang, F. Weng, R. Zou, Q. Liu, *ChemNanoMat* **2024**, 202300558.
- [3] R. Saroha, A. K. Panwar, Y. Sharma, *Ceram. Int.* **2017**, *43*, 5734–5742.
- [4] A. K. Padhi, K. S. Nanjundaswamy, J. B. Goodenough, *J. Electrochem. Soc.* **1997**, *144*, 1188.
- [5] S. Li, H. Zhang, Y. Liu, L. Wang, X. He, *Adv. Funct. Mater.* **2024**, *34*, 2310057.
- [6] S.-Y. Chung, J. T. Bloking, Y.-M. Chiang, *Nat. Mater.* **2002**, *1*, 123–128.
- [7] J. Wang, X. Sun, *Energy Environ. Sci.* **2012**, *5*, 5163–5185.
- [8] Z. Yang, Y. Dai, S. Wang, J. Yu, *J. Mater. Chem. A* **2016**, *4*, 18210–18222.
- [9] V. Aravindan, J. Gnanaraj, Y.-S. Lee, S. Madhavi, *J. Mater. Chem. A* **2013**, *1*, 3518–3539.
- [10] B. Zhang, S. Wang, L. Liu, H. Liu, J. Yang, *Langmuir* **2023**, *39*, 5187–5198.
- [11] W. Yang, Y. Bi, Y. Qin, Y. Liu, X. Zhang, B. Yang, Q. Wu, D. Wang, S. Shi, *J. Power Sources* **2015**, *275*, 785–791.
- [12] J. Zhou, C. Xing, J. Huang, Y. Zhang, G. Li, L. Chen, S. Tao, Z. Yang, G. Wang, L. Fei, *Adv. Energy Mater.* **2023**, 2302761.
- [13] Y. Li, B. Xing, H. Zhang, M. Wang, L. Yang, G. Xu, S. Yang, *RSC Adv.* **2022**, *12*, 26070–26077.
- [14] J. Liu, Y. Wu, B. Zhang, X. Xiao, Q. Hu, Q. Han, L. Wang, F. Bei, X. He, *Small* **2023**, *20*, 2309629.
- [15] H. Zhuang, Y. Bao, Y. Nie, Y. Qian, Y. Deng, G. Chen, *Electrochim. Acta* **2019**, *314*, 102–114.
- [16] S. Guo, H. Shen, Z. Tie, S. Zhu, P. Shi, J. Fan, Q. Xu, Y. Min, *J. Power Sources* **2017**, *359*, 285–294.
- [17] C. Tran, R. Singhal, D. Lawrence, V. Kalra, *J. Power Sources* **2015**, *293*, 373–379.
- [18] P. Yu, Z. Zhang, L. Zheng, F. Teng, L. Hu, X. Fang, *Adv. Energy Mater.* **2016**, *6*, 1601111.
- [19] Z. Ding, L. Zhao, L. Suo, Y. Jiao, S. Meng, Y.-S. Hu, Z. Wang, L. Chen, *Phys. Chem. Chem. Phys.* **2011**, *13*, 15127–15133.
- [20] L. Sun, C. Tian, Y. Fu, Y. Yang, J. Yin, L. Wang, H. Fu, *Chem. Eur. J.* **2014**, *20*, 564–574.
- [21] G. Ferrero, A. Fuertes, M. Sevilla, *J. Mater. Chem. A* **2015**, *3*, 2914–2923.
- [22] P. Hao, Z. Zhao, Y. Leng, J. Tian, Y. Sang, R. I. Boughton, C. P. Wong, H. Liu, B. Yang, *Nano Energy* **2015**, *15*, 9–23.
- [23] L. Zhao, N. Baccile, S. Gross, Y. Zhang, W. Wei, Y. Sun, M. Antonietti, M.-M. Titirici, *Carbon* **2010**, *48*, 3778–3787.
- [24] H. Zhong, P. Zhou, L. Yue, D. Tang, L. Zhang, *J. Appl. Electrochem.* **2014**, *44*, 45–51.
- [25] L. Yue, L. Zhang, H. Zhong, *J. Power Sources* **2014**, *247*, 327–331.
- [26] D. Ding, Y. Maeyoshi, M. Kubota, J. Wakasugi, K. Kanamura, H. Abe, *J. Power Sources* **2020**, *449*, 227553.
- [27] C. F. Armer, M. Lübke, M. Reddy, J. A. Darr, X. Li, A. Lowe, *J. Power Sources* **2017**, *353*, 40–50.
- [28] Y.-K. Hou, G.-L. Pan, Y.-Y. Sun, X.-P. Gao, *ACS Appl. Mater. Interfaces* **2018**, *10*, 16500–16510.
- [29] N. Shi, X. Jiang, Y. Zhang, K. Cheng, K. Ye, G. Wang, D. Cao, *Chem. J. Chin. Univ.* **2015**, *36*, 981–988.
- [30] J.-B. Wu, X. Zhang, M. Ijäs, W.-P. Han, X.-F. Qiao, X.-L. Li, D.-S. Jiang, A. C. Ferrari, P.-H. Tan, *Nat. Commun.* **2014**, *5*, 5309.
- [31] L. An, Z. Li, X. Ren, L. Wang, G. Liang, *Ionics* **2019**, *25*, 2997–3007.
- [32] M. Vezvaei, J. Noël, Z. Tun, D. Shoesmith, *J. Electrochem. Soc.* **2013**, *160*, C414.
- [33] A. La Rue, P. J. Weddle, M. Ma, C. Hendricks, R. J. Kee, T. L. Vincent, *J. Electrochem. Soc.* **2019**, *166*, A4041.
- [34] J. Sun, Z. Li, X. Ren, L. Wang, G. Liang, *J. Alloys Compd.* **2019**, *773*, 788–795.
- [35] Y. Zhu, C. Wang, *J. Phys. Chem. C* **2010**, *114*, 2830–2841.
- [36] K. Tang, X. Yu, J. Sun, H. Li, X. Huang, *Electrochim. Acta* **2011**, *56*, 4869–4875.
- [37] S. J. Shi, J. P. Tu, Y. Y. Tang, Y. Q. Zhang, X. L. Wang, C. D. Gu, *J. Power Sources* **2013**, *240*, 140–148.
- [38] L. Wang, Y. Sun, Y. Li, Z. Xuan, Y. Yao, *Ionics* **2023**, *29*, 4519–4526.
- [39] H. Jin, J. Zhang, L. Qin, Y. Hu, H. Jiang, C. Li, *Ind. Eng. Chem. Res.* **2023**, *62*, 1029–1034.
- [40] L. An, H. Liu, Y. Liu, Z. Li, X. Ren, G. Liang, *J. Alloys Compd.* **2018**, *767*, 315–322.
- [41] Z.-X. Chi, W. Zhang, X.-S. Wang, F.-Q. Cheng, J.-T. Chen, A.-M. Cao, L.-J. Wan, *J. Mater. Chem. A* **2014**, *2*, 17359–17365.

Manuscript received: February 15, 2024

Revised manuscript received: April 12, 2024

Accepted manuscript online: April 15, 2024

Version of record online: May 23, 2024